

Numerical Experiments on Wave Propagation Towards a 3D Null Point Due to Rotational Motions

Galsgaard, K. and Priest, E. R.

Mathematical and Statistical Institute, University of St Andrews, St Andrews, KY16 9SS, FIFE, Scotland

Titov, V. S.

Institute for Theoretical Physics IV, NB 7/31, Ruhr-University Bochum, D-44780 Bochum, Germany

Abstract. We describe 3D resistive MHD numerical experiments at a null point driven by the rotation of magnetic field lines near the spine of the null. When field lines around the spine are rotated, a twist wave propagates in towards the null along field lines and satisfying a Klein-Gordon equation. While the helical Alfvén wave spreads out as the null is approached, a fast-mode wave focuses on the null and wraps around it. Only a weak diffusion of the twisted field line structure is found to take place.

1. Introduction

Magnetic reconnection is a fundamental process in a magnetised plasma for changing the magnetic connectivity of plasma elements and for converting magnetic energy to plasma kinetic energy, heat and fast-particle energy [*Priest & Forbes*, 2000]. In the Sun's atmosphere it is thought to play a key role in heating the corona and producing solar flares. In particular, the role of null points where the magnetic field vanishes, has been highlighted. A key question which we aim to address here and which is important for the potential role of null points in coronal heating and solar flares is: how do external disturbances behave as they propagate in the highly nonuniform vicinity of a null point?

In three dimensions magnetic reconnection may take place either in the absence of a null point or at a null point [e.g., *Schindler et al*, 1988; *Hesse and Schindler*, 1988; *Birn et al*, 1989; *Lau and Finn*, 1991; *Greene*, 1993; *Priest and Démoulin*, 1995; *Wang and Bhattacharjee*, 1996; *Hornig and Rastätter*, 1997, 1998]. The simplest 3D null point has a magnetic field of the form

$$(B_x, B_y, B_z) = \frac{B_0}{L}(x, y, -2z), \quad (1)$$

for which the z -axis represents an isolated field line, known as the *spine*, which approaches the null from above and below [*Priest and Titov*, 1996]. The xy -plane is known as the *fan* of the null and consists of a surface of field lines emanating from the null (Figure 1). *Parnell et al* [1996] have classified more generally the different types of linear null that can exist, while *Titov and Hornig* [2000] have determined their possible steady-state structures.

Priest and Titov [1996] considered the effect of surrounding the null point by a cylindrical surface (with its axis parallel to the spine) and imposing various steady foot-point

Copyright 2002 by the American Geophysical Union.

Paper number .
0148-0227/02/\$9.00

motions on the surface. For example, if the foot-points move uniformly and smoothly across the top and bottom of the cylinder, singular counter-rotational motions are driven at the fan and produce so-called *fan reconnection*. On the other hand, if the foot-points move down on one side of the curved surface and up on the other, *spine reconnection* is driven with singular motions near the z -axis. Exact solutions have been discovered for spine and fan reconnective annihilation [Craig *et al.*, 1995; Craig and Fabling, 1996; Mellor *et al.*, 2002]. Furthermore, several numerical experiments on various aspects of three-dimensional reconnection have been undertaken [e.g., Lau and Finn, 1996; Rickard and Titov, 1996; Galsgaard and Nordlund, 1996, 1997; Galsgaard *et al.* 1996, 1997; Dahlburg *et al.*, 1997; Otto, 1995; Politano *et al.*, 1995; Matthaeus *et al.*, 1996]. Especially the work by Rickard and Titov, (1996) resembles the work presented here. They use the linearised and cold MHD equations in cylindrical coordinates to analyse which perturbations of a single null can accumulate current at the null. They show that only two modes exist, representing current accumulation along the spine axis and in the fan plane of the null respectively.

In the present paper we describe and analyse numerical experiments on the effect of twisting the spine of a null, a perturbation not considered in detail by any of the previous papers. Section 2 presents the equations and numerical setup, while Section 3 describes the spine experiments.

2. Equations and Numerical Setup

For the analytical analysis we adopt the standard MHD equations in the following MKS form for the magnetic field (\mathbf{B}), plasma velocity (\mathbf{v}), plasma pressure (p), density (ρ), temperature (T) and electric current (\mathbf{j})

$$\frac{\partial \mathbf{B}}{\partial t} = \nabla \times (\mathbf{v} \times \mathbf{B}) + \eta \nabla^2 \mathbf{B} \quad (2)$$

$$\rho \frac{D\mathbf{v}}{Dt} = -\nabla p + \mathbf{j} \times \mathbf{B} \quad (3)$$

$$\frac{\partial \rho}{\partial t} = -\nabla \cdot (\rho \mathbf{v}) \quad (4)$$

where $\nabla \cdot \mathbf{B} = 0$ and $\mathbf{j} = \nabla \times \mathbf{B} / \mu_0$.

This section defines the initial condition of the numerical experiment and discusses the method used to investigate the time-dependent evolution of a magnetised plasma containing a single magnetic null point. The plasma is taken to be homogeneous in density and plasma temperature and is initially at rest. The initial magnetic configuration (Eq. (1)) represents a proper potential magnetic null point [Parnell *et al.* 1996] with its spine axis along the z -axis and a symmetric fan in the (x, y) -plane, Fig. 1.

The time-dependent evolution of this configuration driven by time-dependent perturbations imposed on the numerical boundaries of a Cartesian domain is investigated. To follow the dynamical evolution Eq. (3) is replaced by

$$\frac{\partial(\rho \mathbf{v})}{\partial t} = -\nabla \cdot (\rho \mathbf{v} \mathbf{v} + \underline{\underline{\tau}}) - \nabla p + \mathbf{j} \times \mathbf{B}, \quad (5)$$

and an energy equation of the form

$$\frac{\partial e}{\partial t} = -\nabla \cdot (e \mathbf{v}) - p \nabla \cdot \mathbf{v} + Q_{\text{Joule}} + Q_{\text{visc}}, \quad (6)$$

is adopted with velocity \mathbf{v} , thermal energy e , viscous stress

tensor $\underline{\tau}$, gas pressure $p = e(\gamma - 1)$, viscous dissipation Q_{visc} , and Joule dissipation Q_{Joule} , respectively [a basic description of the code and the used expressions is available at <http://www.astro.ku.dk/~kg>, Nordlund and Galsgaard 1997, Caunt and Korpi 2001]. An ideal gas, with $\gamma = 5/3$ is assumed. The equations are non-dimensionalised by setting the magnetic permeability $\mu_0 = 1$, and the gas constant $R_0 = m_u$ (the mean molecular weight). One time unit is equivalent to the Alfvén crossing time of a unit length when both $|\mathbf{B}|$ and ρ are set to 1.

The equations are solved using staggered grids. A sixth-order method is applied to derive the partial derivatives and a fifth-order method is used for doing interpolation. Viscosity and magnetic resistivity are both handled combining a second and a fourth-order method with a discontinuous shock capture mechanism to provide the highest possible spatial resolution for the given numerical resolution. The solution is advanced in time using a third-order predictor-corrector method.

At present closed boundaries are used in the calculations. This implies that the normal component of the velocity is set to zero and that the only velocities in the plane of the boundaries are determined by the imposed boundary conditions described in Eq. (7) below. Waves propagating towards the boundaries are therefore reflected back into the numerical domain.

To provide a perturbation that will accumulate current along the spine axis of the magnetic null point, the magnetic field around the spine axis is perturbed in a rotationally symmetric manner. Using a Cartesian domain the only purely rotational perturbation is one where the spine axis is twisted by a vortex flow centered on the spine axis. Similarly, the null can be perturbed by rotating the fan plane around the spine axis, but this gives a much less clean perturbation due to the imposed boundary conditions and will not be discussed in this paper. For the spine perturbation a vortex flow of the form

$$V(r, t) = 2.26V_0(t) \frac{r}{r_0} \left(1 - \left(\frac{r}{r_0} \right)^4 \right)^2, \quad (7)$$

is imposed on the two z boundaries. Here V_0 is the time-dependent amplitude of the peak velocity, r is the radius, r_0 is the maximum radius of the profile and 2.26 a normalisation constant. Different forms of the time-dependent amplitude modulation are used in various experiments for easier comparison with analytical results.

3. Rotation of the Spine Axis

3.1. Helical Alfvén Waves

One of our experiments is to impose a twisting motion at the top and bottom boundaries of the numerical box and to watch how the twist propagates in along the spine towards the null point, so what do we expect analytically? Suppose the imposed motion is purely azimuthal and consider the equations for a twist wave by linearising about a null point at rest ($\mathbf{v}_0 = 0, \rho_0 = \text{constant}$) in cylindrical polars, namely,

$$\mathbf{B}_0 = \frac{B_0}{L} (R\hat{\mathbf{R}} - 2z\hat{\mathbf{z}}) \quad (8)$$

and assuming perturbations of the form

$$\mathbf{v}_1 = V(R, z, t)\hat{\theta}, \quad \mathbf{B}_1 = B(R, z, t)B_0\hat{\theta}. \quad (9)$$

Then the linearised equations of induction Eq. (2) and motion Eq. (3) become, in the limit of ideal MHD with a uniform pressure,

$$\frac{\partial B}{\partial t} = -2z\frac{\partial V}{\partial z} + R\frac{\partial V}{\partial R} - V, \quad (10)$$

$$\frac{\partial V}{\partial t} = R\frac{\partial B}{\partial R} - 2z\frac{\partial B}{\partial z} + B, \quad (11)$$

in which lengths are measured in terms of L and time in terms of L/v_{A0} , where $v_{A0} = B_0/(\mu_0\rho)^{1/2}$.

Now change variables for the upper half ($z > 0$) of the domain from R and z to $\xi = R^2z$ and $Z = -\frac{1}{2}\log(2z)$, such that the top ($z = \frac{1}{2}$) of the numerical box is given by $Z = 0$. Then Eq. (10) and Eq. (11) simplify to

$$\begin{aligned} \frac{\partial V}{\partial t} &= \frac{\partial B}{\partial Z} + B, \\ \frac{\partial B}{\partial t} &= \frac{\partial V}{\partial Z} - V, \end{aligned}$$

such that the ξ -derivatives are absent. These may in turn be combined to give

$$\frac{\partial^2 V}{\partial t^2} = \frac{\partial^2 V}{\partial Z^2} - V, \quad (12)$$

which is a Klein-Gordon equation.

A useful analytical solution may be found for a propagating wave subject to the initial condition $V = 0$ for all R and Z at $t = 0$ and the boundary condition

$$V = F(R^2)J_0(t) \text{ on } Z = 0 \text{ (} z = \frac{1}{2}\text{)}, \quad (13)$$

where $F(R^2)$ is an arbitrary differentiable function and $J_0(t)$ is the Bessel function. The solution is then

$$V = \begin{cases} F(\psi)J_0[(t^2 - Z^2)^{1/2}], & 0 < Z < t, \\ 0 & Z > t, \end{cases} \quad (14)$$

(where $\psi = 2R^2z$). It represents a twist wave propagating at the Alfvén speed down towards the null point along field lines ($R^2z = \text{constant}$, $\Theta = \text{constant}$). The solution is plotted in Fig. 2, where it can be seen how the wave front propagates along in Z followed by an oscillating Bessel-function wake. In Section 3.3, we shall attempt to see whether a solution that is qualitatively of this form can be obtained by ramping up the boundary velocity quickly to the Bessel-function form Eq. (13).

3.2. Magnetoacoustic Waves in an Axisymmetric Field

Consider next the propagation of linear MHD waves in an axisymmetric potential magnetic field, such as our null point, of the form

$$\mathbf{B}_0 = B_{0R}(R, z)\hat{\mathbf{R}} + B_{0z}(R, z)\hat{\mathbf{z}}$$

under the assumptions that the plasma is ideal and has a uniform density (ρ_0) and that only the Lorentz force is present (i.e., the low-beta limit). In our particular set of experiments $B_{0R} = B_0^*R/L$ and $B_{0z} = -2B_0^*z/L$, but more

generally B_{0R} and B_{0z} satisfy

$$\nabla \cdot \mathbf{B}_0 = 0 \quad \text{and} \quad \nabla \times \mathbf{B}_0 = 0.$$

The linearised equations of induction and motion for perturbations ($\mathbf{v}_1(R, z, t)$ and $\mathbf{B}_1(R, z, t)$) from equilibrium are then

$$\frac{\partial \mathbf{B}_1}{\partial t} = \nabla \times (\mathbf{v}_1 \times \mathbf{B}_0), \quad (15)$$

$$\mu_0 \rho_0 \frac{\partial \mathbf{v}_1}{\partial t} = (\nabla \times \mathbf{B}_1) \times \mathbf{B}_0. \quad (16)$$

In order to satisfy $\nabla \cdot \mathbf{B}_1 = 0$ identically, we write

$$\mathbf{B}_1 = \left(\frac{1}{R} \frac{\partial A_1}{\partial z}, B_{1\phi}(R, z, t), -\frac{1}{R} \frac{\partial A_1}{\partial R} \right) \quad (17)$$

in terms of a flux function $A_1(R, z, t)$ such that $A_0 + A_1 = \text{constant}$ gives the equations of flux surfaces (where $A_0 = B_0^* R^2 z / L$ for our null point).

Then the equations for helical Alfvén-wave and compressional Alfvén wave disturbances in general decouple, as follows. The azimuthal components ($v_{1\phi}$ and $B_{1\phi}$) appear only in the azimuthal (or toroidal) components of Eq. (15) and Eq. (16), namely

$$\frac{\partial B_{1\phi}}{\partial t} = (\mathbf{B}_0 \cdot \nabla) v_{1\phi} - \frac{v_{1\phi} B_{0R}}{R}, \quad (18)$$

$$\frac{\mu_0 \rho_0 \partial v_{1\phi}}{\partial t} = (\mathbf{B}_0 \cdot \nabla) B_{1\phi} + \frac{B_{1\phi} B_{0R}}{R}, \quad (19)$$

and may be combined to give a generalised wave equation, as in Section 3.1.

On the other hand, the remaining components of Eq. (15) and Eq. (16) only involve the R - and z - components of \mathbf{v}_1 and \mathbf{B}_1 and describe compressional Alfvén waves. They imply that

$$\frac{\partial A_1}{\partial t} = -R(v_{1z} B_{0R} - v_{1R} B_{0z}), \quad (20)$$

$$\frac{\partial v_{1R}}{\partial t} = \frac{B_{0z}}{\mu_0 \rho_0} \Delta^* A_1, \quad (21)$$

$$\frac{\partial v_{1z}}{\partial t} = -\frac{B_{0R}}{\mu_0 \rho_0} \Delta^* A_1, \quad (22)$$

where $\Delta^* A_1 = R^{-1} \partial^2 A_1 / \partial z^2 + \partial / \partial R (R^{-1} \partial A_1 / \partial R)$. Eliminating v_{1R} and v_{1z} gives a generalised wave equation of the form

$$\frac{\partial^2 A_1}{\partial t^2} = v_{A0}^2 \left(\frac{\partial^2 A_1}{\partial z^2} + \frac{\partial^2 A_1}{\partial R^2} - \frac{1}{R} \frac{\partial A_1}{\partial R} \right), \quad (23)$$

where $v_{A0}(R, z) = B_0(R, z) / (\mu_0 \rho)^{1/2}$ is the Alfvén speed and $B_0^2 = B_{0R}^2 + B_{0z}^2$ so that $v_{A0}^2 = v_{A0}^{*2} (R^2 + 4z^2) / L^2$, where $v_{A0}^* = B_0^* / (\mu_0 \rho)^{1/2}$. We notice that the Alfvén speed vanishes at the null point and so any magneto-sonic part of the disturbance originating from the boundaries or from coupling in the volume is likely to approach the null and to accumulate there.

The way that this occurs may be modelled by supposing

$$A_1 = A_{10} e^{i(\omega t v_{A0}^* / L + u)}$$

where A_{10} is a constant amplitude, ω is the dimensionless

frequency and $u = u(R, z)$. Eq. (23) then becomes

$$(R^2 + 4z^2) \left[\left(\frac{\partial u}{\partial R} \right)^2 + \left(\frac{\partial u}{\partial z} \right)^2 - i \frac{\partial^2 u}{\partial R^2} - i \frac{\partial^2 u}{\partial z^2} + \frac{i}{R} \frac{\partial u}{\partial R} \right] - \omega^2 = 0 \quad (24)$$

Next we make a usual WKB approximation by assuming $u \approx \omega \gg 1$, while R and z are of order L , so that u varies slowly over a wavelength and $(\partial u / \partial R)^2 \approx (\partial u / \partial z)^2 \gg \partial^2 u / \partial R^2 \approx \partial^2 u / \partial z^2 \approx \frac{1}{R} \partial u / \partial R$. Then Eq. (24) may be approximated to lowest order by

$$F(R, z, u, p, q) = (R^2 + 4z^2)(p^2 + q^2) - \omega^2 = 0, \quad (25)$$

where $p = \partial u / \partial R$, $q = \partial u / \partial z$. The standard characteristic equations for Eq. (25) are then

$$\frac{\partial R}{\partial s} = 2(R^2 + 4z^2)p, \quad (26)$$

$$\frac{\partial z}{\partial s} = 2(R^2 + 4z^2)q, \quad (27)$$

$$\frac{\partial p}{\partial s} = -2R(p^2 + q^2), \quad (28)$$

$$\frac{\partial q}{\partial s} = -8z(p^2 + q^2), \quad (29)$$

together with

$$\frac{\partial u}{\partial s} = 2\omega^2, \quad (30)$$

which implies $u = 2\omega^2 s + \text{constant}$, so that u increases linearly with s along a characteristic curve. Taking p times Eq. (26), q times Eq. (27), R times Eq. (28), z times Eq. (29) and adding gives

$$\frac{\partial}{\partial s} (Rp + qz) = 0, \quad (31)$$

so that an integral of the set Eq. (26) - (29) is

$$Rp + zq = q_0, \quad (32)$$

where q_0 is a constant. If we suppose that $p = 0$ and $q = q_0$ at $R = R_0$, $z = z_0$, then from Eq. (25)

$$q_0 = \frac{\omega^2}{R_0^2 + 4z_0^2}. \quad (33)$$

The characteristic curves in the Rz -plane are then determined by Eq. (25), Eq. (29) and

$$\frac{\partial R}{\partial z} = \frac{p}{q}. \quad (34)$$

Close to the point (R_0, z_0) the behaviour of the characteristic may be found by linearising these equations to give

$$R \approx R_0 - \frac{\frac{1}{2}R_0}{R_0^2 + 4z_0^2} (z - z_0)^2, \quad (35)$$

so that the characteristics curve towards the origin as z decreases at a rate which increases with R_0 from zero to a maximum value at $R_0 = 2z_0$ and then decreases to zero as R_0 increases further. A numerical solution to Eq. (26) - (29) is shown in Fig. 3. Here we start with a wave-front as a line at $z_0 = 0.5$ and follow how it accumulates at and

wraps around the null point as a function of time.

3.3. Numerical Results

The first numerical experiment is set up to compare directly with the analytical results provided in Section 3.1. The analytical solution there initiates a wave with a discontinuity in the driving velocity on the z boundaries, starting initially with zero velocity in the domain and then on the boundaries having a peak velocity of the driving function given by Eq. (7). Numerically this provides a difficulty and instead the driving velocity is ramped up over a short time-scale to prevent numerical overshooting due to the discontinuity. Fig. 4 shows how the perturbation propagates into the numerical domain along a magnetic field line as a function of time. The individual curves in the figure represent the rotational velocity along a magnetic field line at different times after the imposed boundary driving is switched on. Comparing this figure with the result from the Klein-Gorden equation shown in Fig. 2, shows similar features for small velocity perturbation amplitudes. The main difference is that the amplitude of the numerical result decreases with time. This is a result of diffusing the steep initial profile with time. At the same time, the numerical resolution becomes critical as $Z = -0.5 \log(z)$ increases. Here the distance to the fan plane decreases and the resolution in this direction is limited by the uniform grid.

The panels in Fig. 5 compare the Klein-Gordan shape of a wave propagating into the domain with the numerical MHD solution, but this time the amplitude is slowly increased from zero, with the corresponding numerical result. In this case the comparison between the Klein-Gordan and MHD solution is much better. This is due to the lack of a discontinuity of the imposed driving velocity. This similarity has encouraged us to extend the analysis of the numerical experiments further.

There are two ways in which driving can be imposed on the two z boundaries, namely with similar or opposite vorticity of the two imposed boundary perturbations. When the two driving flows have the same vorticity, then a current, j_z , of same sign is generated at both driving boundaries and one could assume that this current structure would carry through the null point. In the case where the driving flows have opposite vorticity, the direction of the current, j_z , will be of opposite sign at the two driving boundaries and no current will pass through the null point; instead a strong current in the fan plane is expected. In the following, both cases are investigated in more detail.

First, we analyse the propagation of current into the numerical domain for the two cases. In Fig. 6 the current structure is shown for five different times for the case where the drivers have the same vorticity. The panels represent time in the vertical direction and the three current components and its magnitude in the horizontal direction. The 2D plane includes the null point at the centre. The panels in the horizontal strip represent, from left to right, the component out of the plane, the horizontal component, the vertical component and the magnitude of the current. These panels are scaled to their maximum and minimum values at each time step to provide the largest contrast for each component. By comparing with the magnitude of the current an idea of their relative importance at each time can be found. The sharp front seen in the x -component of the current is generated by the very fast ramp-up of the

driving velocity. The y -component is weaker than the others and represents a small perturbation of the current. For this component we have to notice the tendency to have a wave propagating faster than the Alfvén speed converging towards the null point. This is the fast-mode wave discussed in Section 3.2. Finally, the z -component of the current contains the main current of the system – the current associated with the twist of the magnetic field. Here it is seen that the current consist of two contributions, namely a “black” component and a “white” component. These are of opposite sign, and while the “black” represents the internal twist of the magnetic field the “white” is generated because the driving profile goes to zero at a finite radius. From the panels it is obvious that no strong current penetrates the null point or accumulates in the fan plane at any time for this imposed driving.

Similar to the current shown in Fig. 6 a display of the velocity evolution is shown in Fig. 7. This shows that the dominating velocity component in the yz -plane is the y -component, the vorticity component imposed by the driving field on the boundaries, while the x - and z -velocities are small compared to this. This agrees well with the analytical investigation where these components have zero amplitude. Towards the end of the time series a rotational velocity disk is formed around the null in the fan plane with a vorticity that is opposite to the imposed driving. The reason for the development of this vortex disk is not obvious, as effects from both the imposed boundaries and diffusion at the null point and fan plane may influence its creation.

In Fig. 8 the time-dependent changes in the field line connectivity are shown. A number of magnetic field lines are traced from fixed starting points on the top z -boundary. This implies that the traced field lines will rotate around the spine axis as the twist is imposed by the driving flow on the z boundary. In the ideal case they should then keep their foot-point distribution at the boundaries when the driving amplitude goes to zero after a fixed time. In Fig. 8 it is seen, however, that this is not the case. The behaviour of the field lines with large starting radii is close to the ideal picture. As the distance to the spine axis decreases, the diffusion effect increases and seems to reach a maximum at a relatively large radius, namely, where the most rapid change in the imposed velocity is found. For smaller radii the change in field line connectivity decreases again and shows only a small affect from diffusion.

In the second experiment the driving velocity on the top z -boundaries is reversed relative to the experiments discussed above. In this case the current accumulation due to the fast rise in driving velocity has the opposite sign on either side of the fan plane. As this perturbation reaches the fan plane the current from the two sides combines into one strong current concentration located in the fan plane away from the null point. Again we notice the presence of the fast-mode wave that is being “caught” by the null and wraps around it generating an interesting wave pattern that seems to be confined to the region of field lines perturbed by the boundary driving.

By comparing the phase of the perturbation in the magnetic field and in pressure, it is confirmed that the wave propagating towards the null is indeed a fast-mode wave, since their perturbations are in phase. The driving of the fast-mode wave is likely to be a nonlinear coupling of the helical Alfvén wave (e.g., *Nakariakov et al*, [1997]). This

non-linear mode coupling of the the fast-mode wave was not anticipated by *Rickard and Titov* (1996), as their analysis was conducted in the linear approximation ignoring the plasma pressure. Thus in the linear regime a $j_R B_\phi$ -part of the Lorentz force will drive a z -component of velocity in the equation of motion. By comparing any of the images representing the current or velocity in the experiments with the analytical structure of the fast-mode wave in Fig. 3, one unanswered question arises. When solving the characteristic equations, Eq. (26) - (29), it was found that the length of the initial front decreases with time and eventually vanishes into the null point. In the full MHD experiment the fast-mode front continues to extend all the way out to the field line envelope defined by the field lines just outside the region perturbed by the vortex boundary motion. In other words, the length of the fast-mode front continuously changes to reach this boundary. How does it “prevent” the shrinking effect and how does it “know” that this is the outer boundary? In the experiments where the boundary velocity is slowly increased, we are not able to identify the presence of the fast-mode wave. The near discontinuity in the boundary driving velocity is therefore important for the generation and identification of the fast-mode wave as the weak non-linear coupling between the twist wave and the fast-mode wave is largest for this case.

Fig. 10 shows only the three latest panels of the velocity for this case. By comparing with Fig. 7 it is noticed that the velocity patterns are very similar, except for the y -component in the last panel. Here this experiment lags the vortex disk that developed in the former case in the fan plane around the null point.

Field line traces for this experiment are shown in Fig. 11. Looking at the time series it is seen that the field lines in this experiment do not lose a significant amount of their twist with time. Their connectivity is better maintained than in the previous case.

4. Conclusions

Both the analytical and numerical investigations of the vortex perturbation of a 3D null point spine axis show how a twist wave propagates along the magnetic field lines towards the fan plane. As it approaches the fan plane the twist wave spreads out along the diverging field lines on either side of the fan plane and momentarily produces a current accumulation in the fan plane. The strength and duration of the current structure depends critically on the imposed twist around the two spine axes. The strongest current is generated when the twist of field lines on both spine axes have opposite directions. As most of the perturbed field lines do not come within a given small distance from the null point, most of the current concentration is located away from the null point, even in the case where the direction of the current along both spine axes have the same direction. Diffusion of the magnetic field lines through the plasma is therefore limited and only a very small fraction of the imposed twist is released in the experiment.

Apart from the twist wave, which in its pure form is a helical Alfvén wave, nonlinear effects generate a fast-mode wave. In the case of the near discontinuous rise of the driving velocity, the fast-mode-wave moves ahead of the Alfvén wave as the null is approached and focuses its energy at the null point. The major part of the energy that reaches a small

neighbourhood of the null point is advected there by the fast-mode wave. The energy of the fast-mode wave is small compared to the twist wave. The effect it has on the field line structure is therefore very limited.

This vortex perturbation of the spine axis of a magnetic null is not the only way to stress a single null. A general perturbation would include also a compression or expansion together with an advection. In future papers we intend to investigate the implication of such motions on the dynamical evolution of a 3D null point.

Acknowledgments. We are greatfull to Alan Hood and Valera Nakariakov for helpful comments. K. Galsgaard was supported by PPARC in the form of an Advanced Fellowship. The numerical MHD experiments were carried out using the PPARC-funded Compaq MHD Cluster in St. Andrews. This work was supported in part by the European Community's Human Potential Program under contract HPRN-CT-2000-00153, PLATON and by the Volkswagen-Foundation. We thank the two unknown referees for their help in improving the paper.

References

- Birn, J., Hesse, M. and Schindler, K. (1989) Filamentary structure of a three-dimensional plasmoid, *J. Geophys. Res.* **94**, 241–251.
- Caunt, S. E. and Korpi, M. J. (2001) A 3D MHD model of astrophysical flows: Algorithms, tests and parallisation, *A & A* **369**, 706–728
- Craig, I.J.D. and Henton, S.M. (1995) Exact solutions for steady-state incompressible magnetic reconnection, *Astrophys. J.* **450**, 280–288.
- Craig, I.J.D. and Fabling, R.B. (1996) Exact solutions for steady-state spine and fan magnetic reconnection, *Astrophys. J.* **462**, 969–976.
- Dahlburg, R.B., Antiochos, S.K. and Norton, D. (1997) Magnetic flux tube tunnelling, *Phys. Rev. E* **56**, 2094–2103.
- Galsgaard, K. and Nordlund, Å. (1996) Heating and activity of the solar corona. 1. Boundary Shearing of an Initially Homogeneous Magnetic Field *J. Geophys. Res.* **101**, 13445–13460.
- Galsgaard, K. and Nordlund, Å. (1997) Heating and activity of the solar corona. 3. Dynamics of a low-beta plasma with three-dimensional null points, *J. Geophys. Res.* **102**, 231–248.
- Galsgaard, K., Rickard, G.J., Reddy, R.V. and Nordlund, Å. (1996) Dynamical Properties of Single and Double 3D Null Points, *ASP Conference Proceedings*, **111**, 82–88.
- Galsgaard, K., Rickard, G.J. and Reddy, R.V. (1997) Energy Release Sites in Magnetic Fields Containing Single or Multiple Nulls *Sol. Phys.*, **176**, 299–325.
- Greene, J.M. (1993) Reconnection of vorticity lines and magnetic lines, *Phys. Fluids B* **5**, 2355–2362.
- Hesse, M. and Schindler, K. (1988) A theoretical foundation of general magnetic reconnection, *J. Geophys. Res.* **93**, 5539–5567.
- Hornig, G. and Rastätter. (1997) The role of helicity in the reconnection process, *Adv. Space Res.* **19**, 1789–1792. *J. Geophys. Res.* **100**, 23,443–23,463.
- Hornig, G. and Rastätter. (1998) The magnetic structure of $B \neq 0$ reconnection, *Physica Scripta* **T74**, 34–39.
- Lau, Y.-T. and Finn, J.M. (1991) Three-dimensional kinematic reconnection of plasmoids, *Astrophys. J.* **366**, 577–599.
- Lau, Y.-T. and Finn, J.M. (1996) Magnetic reconnection and the topology of interacting twisted flux tubes, *Phys. Plasmas* **3**, 3983–3997.
- Matthaeus, W.H., Ghosh, S., Oughton, S. and Roberts, D.A. (1996) Anisotropic three-dimensional MHD turbulence, *J. Geophys. Res.* **101**, 7619–7629.
- Mellor C., Priest, E. R. and Titov, V. S. (2002) Exact Solutions for Spine Reconnective Magnetic Annihilation, *Geophys Astrophys. Fluid Dynamics*, inpress.
- Nakariakov, V. M. Roberts, B. and Murawski, K. (1997) *Solar Phys.* **175**, 93–105.

- Nordlund, Å. and Galsgaard, K. (1997) *Tech. Rep.* Astronomical Observatory, Copenhagen University
- Otto, A. (1995) Forced three-dimensional magnetic reconnection due to linkage of magnetic flux tubes, *J. Geophys. Res.* **100**, 11863–11874.
- Parnell, C.E., Smith, J., Neukirch, T. and Priest, E.R. (1996) The structure of three-dimensional magnetic neutral points, *Phys. Plasmas* **3**, 759–770.
- Politano, H., Pouquet, A. and Sulem, P.L. (1995) Current and vorticity dynamics in three-dimensional magnetohydrodynamic turbulence, *Phys. Plasmas* **2**, 2931–2939.
- Priest, E.R. and Démoulin, P. (1995) Three-dimensional reconnection without null points, *J. Geophys. Res.* **100**, 23443–23463.
- Priest, E.R. and Forbes, T. (2000) *Magnetic Reconnection, MHD theory and applications* Cambridge University Press, ISBN 0-521-48179-01
- Priest, E.R. and Titov, V.S. (1996) Magnetic reconnection at three-dimensional null points, *Phil. Trans. Roy. Soc. Lond. A* **354**, 2951–2992.
- Rickard, G. J. and Titov, V. S. (1996) Current Accumulation at a Three-Dimensional Magnetic Null *ApJ*, **472**, 840–852.
- Schindler, K., Hesse, M. and Birn, J. (1988) General magnetic reconnection, parallel electric fields and helicity, *J. Geophys. Res.* **93**, 5547–5557.
- Titov, V. S. and Hornig, G. (2000) MHD Flows Sustaining Stationary Magnetic Nulls, *Phys. Plasmas* **7**, 3542–3350.
- Wang, X. and Bhattacharjee, A. (1996) A three-dimensional reconnection model of the magnetosphere: Geometry and kinematics, *J. Geophys. Res.* **101**, 2641–2653.

Galsgaard, K. and Priest, E. R., Mathematical and Statistical Institute, University of St Andrews, St Andrews, KY16 9SS, FIFE, SCOTLAND (klaus@mcs.st-and.ac.uk and eric@mcs.st-and.ac.uk)

Titov, V. S., Institute for Theoretical Physics IV, NB 7/31, Ruhr-University Bochum, D-44780 Bochum, Germany (st@tp4.ruhr-uni-bochum.de)

(Received March 2002; revised 2002; accepted 2002.)

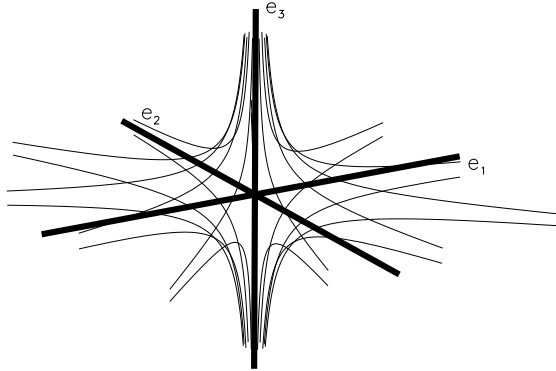


Figure 1. The structure of a 3D null point. The direction indicated by \mathbf{e}_3 vector represents the spine axis, while the plane defined by \mathbf{e}_1 and \mathbf{e}_2 defines the fan plane. Notice that a proper null is rotationally symmetric around the spine axis.

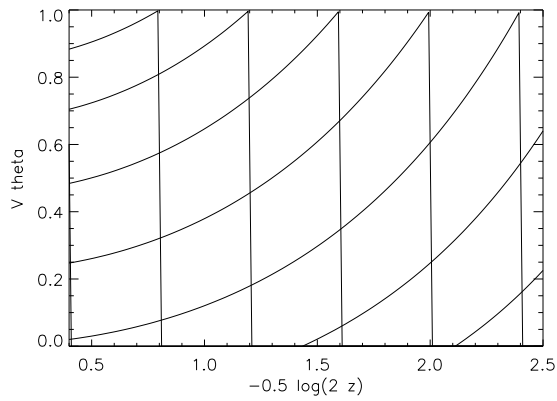


Figure 2. The velocity profile (V_θ) of a twist wave as a function of z for several different times given by Eq. (14). The different curves represent different times with the wave-front propagating to the right with time. Notice the maintained maximum velocity at the front and the subsequent decay in amplitude on the driving boundary, $Z = -0.5 \log(2z)$.

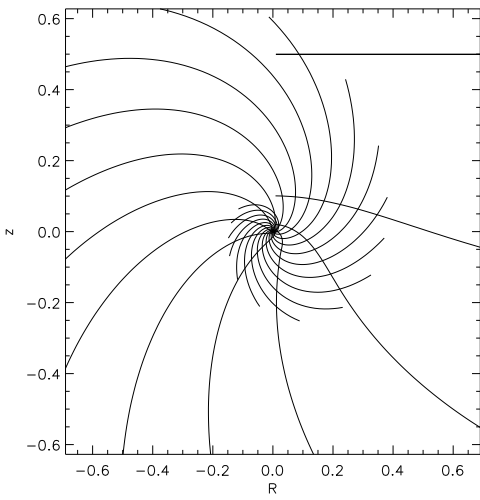


Figure 3. The solution to the characteristic equations, Eq. (26) - (29) in the Rz -plane. The solution is integrated from $z = 0.5$ with R values between $[0, 2.5]$, $p = 0$ and using Eq. (33) to determine q with $\omega = 1$. The lines show how the fronts propagate in time, wrapping around the null point as it contracts towards it.

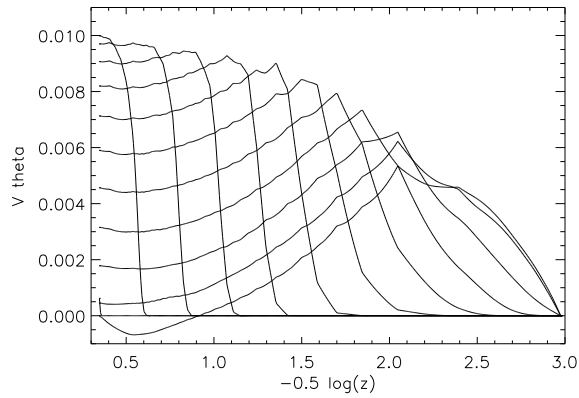


Figure 4. The rotational velocity along a magnetic field line at different times. The results are to be compared with the curves in Fig. 2.

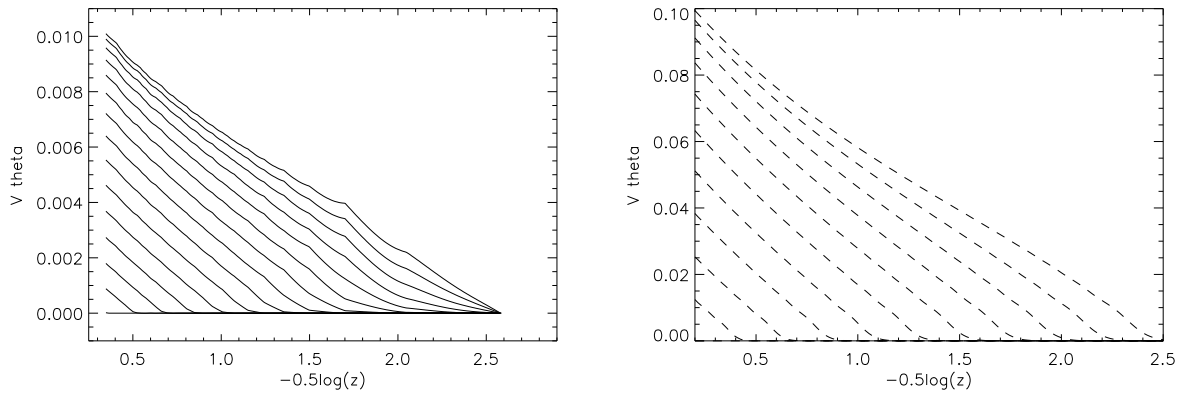


Figure 5. Graphs similar to Fig. 2 and Fig. 4. Here the driving is without the initial discontinuity at the top boundary. The left panel is the numerical solution to Eq. (12), while right panel is the 3D MHD solution.

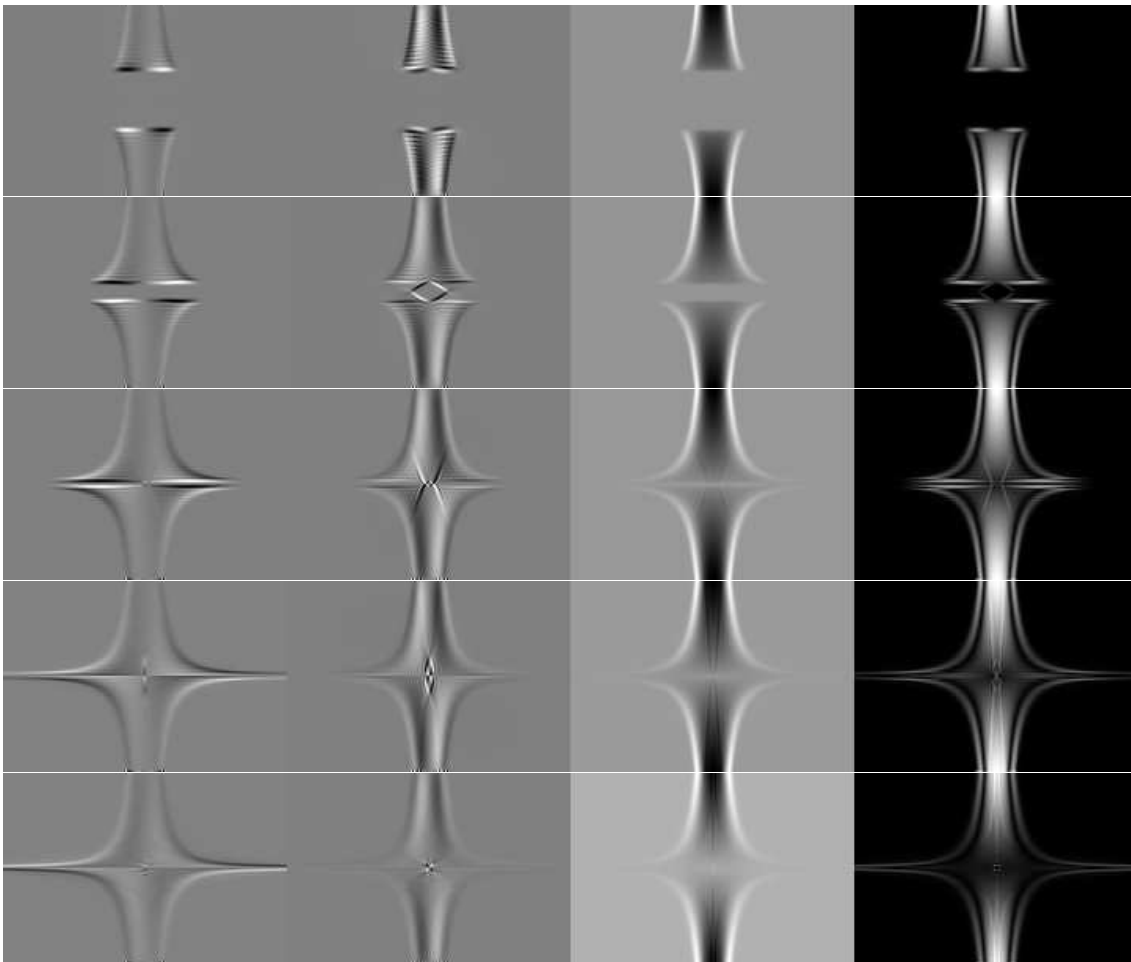


Figure 6. The panels represent the current structure at five equidistant times of the evolution in the yz -plane including the null point. In the horizontal direction the panels represent the x , y and z -components of the current and the current magnitude. Each frame is scaled to its own minimum and maximum values at each frame. This enhances the contrast of the frames, but makes comparisons between them difficult.

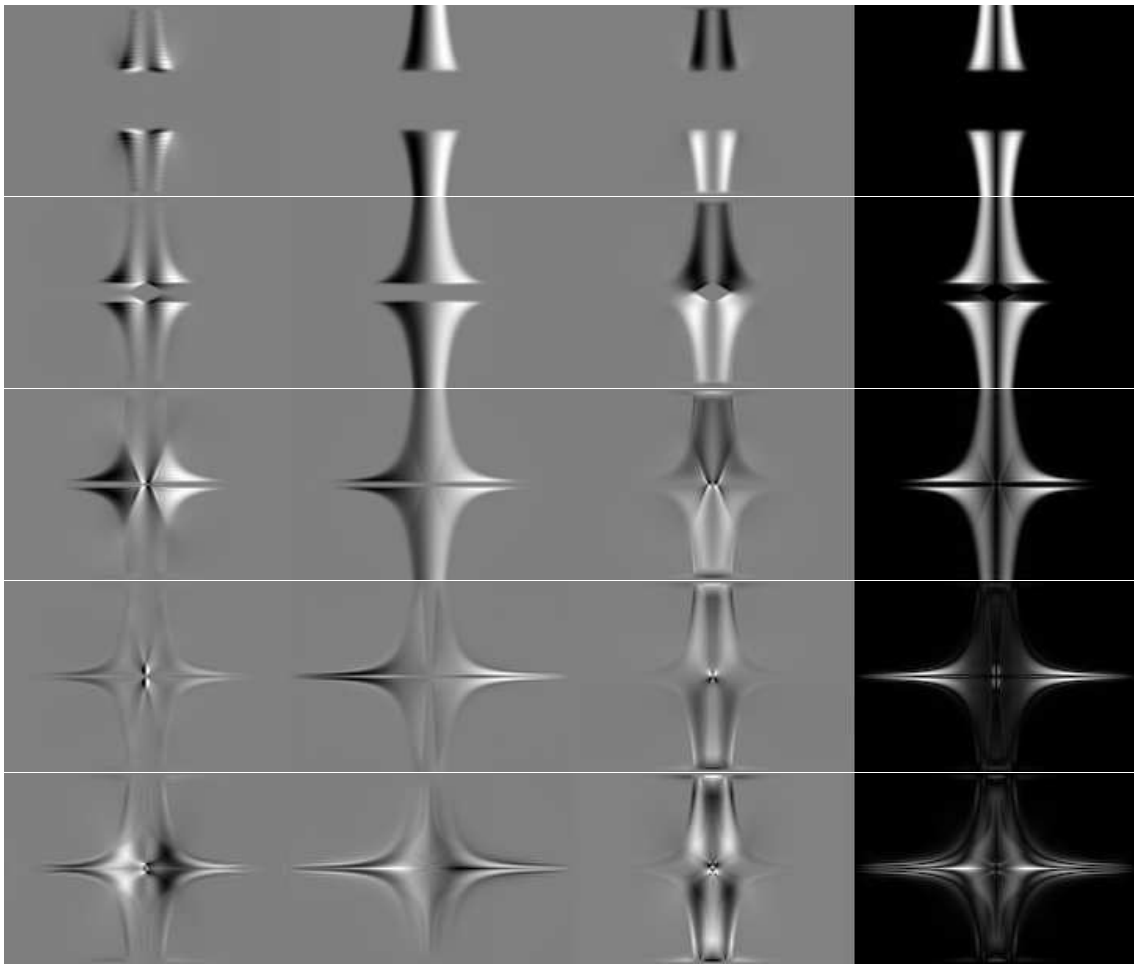


Figure 7. The time development of the velocity field is shown in a similar manner to the current in Fig. 6.

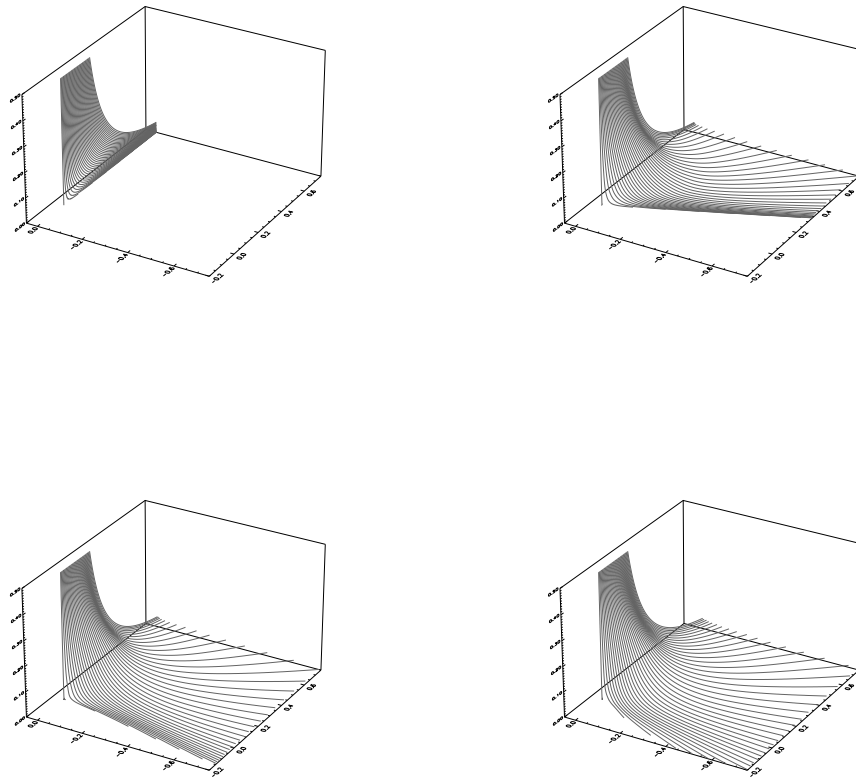


Figure 8. Magnetic field line traces as a function of time from fixed starting point on the top boundary. The panels represent the evolution at times 0.00, 1.18, 2.36, and 3.78 respectively.

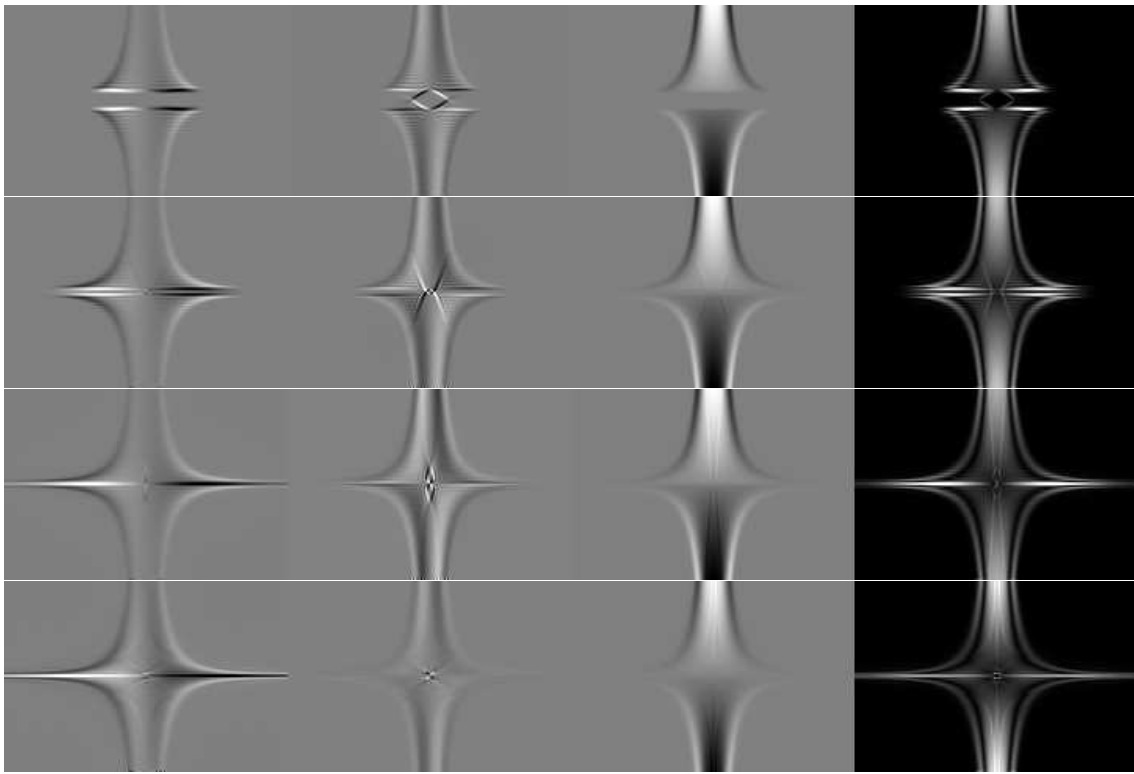


Figure 9. Current plots similar to Fig. 6. Notice the reversal of the z -current in the upper half of the domain and the strong current accumulation in the fan plane as the two pulses reach the fan plane.

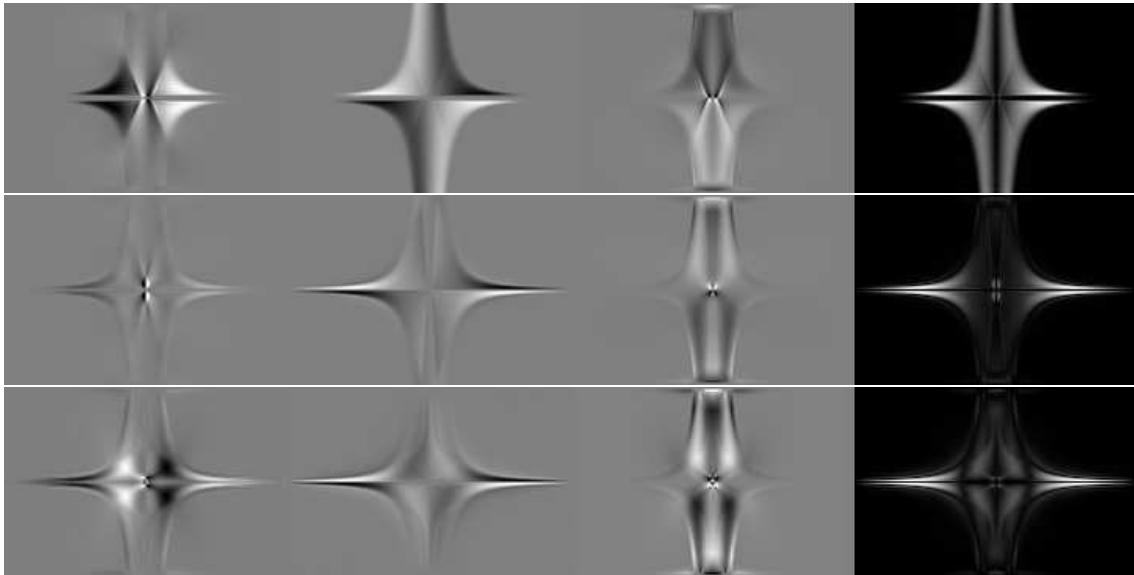


Figure 10. Velocity plots similar to Fig. 7. Notice the reversal of the y -velocity in the upper half of the domain.

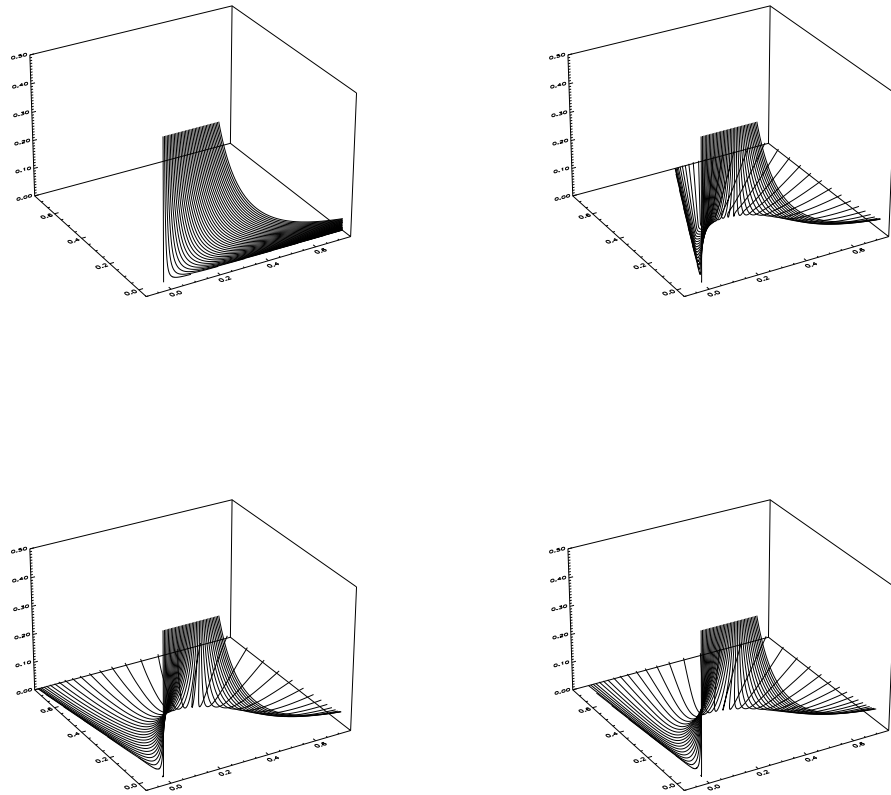


Figure 11. Field line traces showing how the structure of the magnetic field line connectivity changes as a function of time. The panels represent the evolution at times 0.00, 1.18, 2.37, and 3.79 respectively.